



**HAL**  
open science

## Viscous roots of active seismogenic faults revealed by geologic slip rate variations

P.A. Cowie, C.H. Scholz, G.P. Roberts, G.P. Faure Walker, Philippe Steer

► **To cite this version:**

P.A. Cowie, C.H. Scholz, G.P. Roberts, G.P. Faure Walker, Philippe Steer. Viscous roots of active seismogenic faults revealed by geologic slip rate variations. *Nature Geoscience*, 2013, 6, pp.1036-1040. 10.1038/NGEO1991 . insu-00913173

**HAL Id: insu-00913173**

**<https://insu.hal.science/insu-00913173>**

Submitted on 8 Jul 2014

**HAL** is a multi-disciplinary open access archive for the deposit and dissemination of scientific research documents, whether they are published or not. The documents may come from teaching and research institutions in France or abroad, or from public or private research centers.

L'archive ouverte pluridisciplinaire **HAL**, est destinée au dépôt et à la diffusion de documents scientifiques de niveau recherche, publiés ou non, émanant des établissements d'enseignement et de recherche français ou étrangers, des laboratoires publics ou privés.

1 **Viscous roots of active seismogenic faults revealed by geologic slip rate**  
2 **variations**

3 **P. A. Cowie<sup>1</sup>, C. H. Scholz<sup>2</sup>, G. P. Roberts<sup>3</sup>, J. P. Faure Walker<sup>4</sup> and P. Steer<sup>1,5</sup>**

4 1. Department of Earth Science, University of Bergen, Bergen 5002, Norway

5 2. Lamont Doherty Earth Observatory of Columbia University, Palisades, NY 10964-8000, USA

6 3. School of Earth Sciences, Birkbeck College, University of London, WC1E 7HX, UK

7 4. Institute for Risk and Disaster Reduction, University College London, London, WC1E 6BT, UK

8 5. Géosciences Rennes, Université de Rennes 1, CNRS, Rennes Cedex CS 35042, France.

9 **During the earthquake cycle viscous flow at depth contributes to elastic strain**  
10 **accumulation along seismogenic faults<sup>1</sup>. Evaluating the importance of this contribution**  
11 **to fault loading is hampered by uncertainty about whether viscous deformation mainly**  
12 **occurs in shear zones or by distributed flow. Furthermore, viscous strain rate has a**  
13 **power-law dependence on applied stress<sup>2</sup> but few estimates exist for the power-law**  
14 **exponent applicable to the long term in situ behaviour of active faults. Here we show**  
15 **that measurements of topography and whole-Holocene offsets along seismically active**  
16 **normal faults in the Italian Apennines can be used to derive a relationship between**  
17 **stress and strain rate (averaged over  $15\pm 3$  kyrs). This relationship, which follows a well-**  
18 **defined power-law with an exponent in the range 3.0-3.3 ( $1\sigma$ ), is used to infer the**  
19 **rheological structure of the crust and constrain the width of active extension across the**  
20 **Apennines. Our result supports the idea that the irregular, stick-slip movement of**  
21 **upper crustal faults, and hence earthquake recurrence, are controlled by down-dip**  
22 **viscous flow in shear zones over multiple earthquake cycles.**

23 Earthquakes in the crust occur down to depths of approximately 15km in most regions  
24 because below this depth temperature- and time-dependent creep (aseismic) deformation  
25 processes become progressively more important. It is therefore generally accepted that the  
26 upper crustal, seismogenic, portion of a fault is rooted down dip into a ductile (mylonitic)  
27 shear zone and that the transition from frictional stick-slip to viscous flow is temperature and  
28 strain rate dependent. At sufficiently high temperatures, distributed ductile deformation may  
29 also occur in the lower crust and upper mantle. *Both* localised flow in shear zones and  
30 distributed flow lead to elastic strain accumulation in the upper crust and thus loading of  
31 faults to failure but currently there is disagreement as to which dominates<sup>3,4</sup>. Experimental  
32 work, field data and theory indicate the flow law for the lithosphere at tectonic strain rates  
33 should be that of dislocation creep in which strain rate,  $\dot{\epsilon}$ , is proportional to stress raised to an  
34 exponent  $n$ , where  $n$  is typically in the range 2 to 4<sup>5,6</sup>:

$$35 \quad \dot{\epsilon} = A\sigma^n \exp\left(-\frac{Q}{RT}\right) \quad \text{Equation 1}$$

36 Here  $\sigma$  is driving stress,  $A$  is a material property,  $Q$  is activation energy,  $R$  is the molar gas  
37 constant and  $T$  is absolute temperature. Geodetic observations of post-seismic relaxation  
38 reveal temporal and spatial variations in effective viscosity that are most easily explained by  
39 power law creep with  $n \approx 3$ <sup>7</sup>. However geodetic data generally do not permit discrimination  
40 between contributions of bulk flow of the upper mantle, of the lower crust, or plastic creep  
41 within a shear zone<sup>2</sup>. Moreover, it is not clear that the rheological properties indicated by  
42 postseismic transients are applicable to longer term behaviour of the coupled frictional-  
43 viscous fault system<sup>8</sup>.

44 Here we show that extensional strain rates derived from slip on seismogenic normal  
45 faults in the actively uplifting and extending central and southern Italian Apennines can be

46 used to address this issue. The strain rates are measured at the surface using published  
47 structural data<sup>9,11</sup> (Fig. 1, 2; see Methods) along active normal faults, characterised by  
48 bedrock scarps that exhibit striated fault planes and offset dated Holocene sediments and  
49 geomorphic surfaces<sup>11</sup>. These faults have developed in the last 2-3 My since thrusting in this  
50 region diminished as westward subduction of the Adriatic plate beneath the Italian peninsula  
51 slowed and slab tearing/detachment initiated  $\sim 6$  Ma<sup>10,12</sup>. Present day topographic elevation  
52 increases inland reaching elevations up to 2900 m locally along the footwall crests of major  
53 extensional faults. Short wavelength (10-20 km) topographic variations due to faulting are  
54 superimposed on long wavelength (100-150 km) topography aligned NW-SE along the axis  
55 of the Italian Peninsula<sup>12</sup> (Fig. 2a). Gravity admittance data indicate that the long wavelength  
56 topography is supported by buoyancy variations in the uppermost mantle<sup>12</sup>. Regional surface  
57 uplift rates<sup>13</sup> increase in magnitude inwards from the Adriatic and Tyrrhenian coasts,  
58 mimicking in shape the long wavelength topography<sup>13</sup>.

59         The extensional strain rates, averaged over the whole Holocene ( $15 \pm 3$  kyrs), correlate  
60 with average topographic elevation along the length of the central and southern Apennines<sup>10</sup>  
61 (Fig. 1c). This observation is confirmed by the map view distribution of active faults relative  
62 to topographic contours (e.g., Fig. 2a). Geodetic data also show that the highest contemporary  
63 strain rates coincide with the highest elevation area in the central Apennines<sup>14</sup>. A power law  
64 regression between the strain rate,  $\dot{\epsilon}$ , and elevations,  $h$ , (in transects 90 km across strike by 30  
65 km wide along strike) reveals a well-defined relationship with power law exponents in the  
66 range 3.0-3.3 ( $1\sigma$ ) (see Methods and Supplementary material). Data from two independent  
67 sets of 30km transects show that the result is not location dependent (Fig. 1d). Varying  
68 transect width (from 5 km to 60 km) shows that over all scales the exponent lies within the  
69 range 2.7-3.4 and 2.3-4.0 at 95% and 99% confidence intervals respectively. These variations

70 in strain rate cannot be attributed to thermal structure as heat flow increases gradually from <  
71  $40 \text{ mWm}^{-2}$  along the Adriatic coast to  $> 60 \text{ mWm}^{-2}$  along the Tyrrhenian coast, independent  
72 of elevation and distance along strike<sup>15</sup>.

73 To interpret our data (Fig. 1d) in terms of Equation 1 we need to demonstrate that  $h$   
74 and  $\sigma$  are directly proportional. Previous workers (e.g., ref **16**) made the connection by  
75 approximating the lithosphere as a homogeneous thin viscous sheet. However, where thicker  
76 than average crust (40 – 50km) overlies thinned mantle lithosphere, as it does in the central  
77 and southern Apennines, the vertical velocity field is unlikely to be continuous at the scale of  
78 the entire lithosphere<sup>17</sup>. Furthermore, the topography varies by 100's of meters over  
79 wavelengths  $< 100 \text{ km}$  in which case approximations made in the thin sheet model break  
80 down<sup>18</sup>. To avoid making these approximations we use observational constraints to relate  $h$  to  
81  $\sigma$  by noting that (1) the upper crust is at or close to the threshold for brittle failure, i.e., “at  
82 yield”<sup>19</sup> and (2) earthquake focal mechanisms and fault kinematic data along active faults<sup>9,11</sup>  
83 indicate that the maximum compressive stress,  $\sigma_1$ , is vertical and the least compressive  
84 stress  $\sigma_3$  is parallel to the principal extensional strain orientation (NE-SW in Fig. 2). In an  
85 elastic-brittle upper crust at yield,  $\sigma_3$ , is directly proportional to  $\sigma_1$ , compatible with incipient  
86 frictional failure on optimally oriented planes<sup>20</sup> (Fig. 3). Thus the differential stress is also  
87 proportional to  $\sigma_1$ , e.g.,  $(\sigma_1 - \sigma_3) \approx 2\sigma_1/3$  if Byerlee friction constants are assumed. Below the  
88 base of the seismogenic zone ( $\sim 14\text{-}17 \text{ km}$  depth in this region<sup>19,21</sup>), where viscous flow  
89 dominates, differential stress is less but we assume there is no stress discontinuity across this  
90 transition over long time scales (Fig. 3). Additional topographic loads that result from surface  
91 uplift relative to sea level increase  $\sigma_1$ , and hence  $(\sigma_1 - \sigma_3)$ , driving deformation (by a depth  
92 and temperature dependent combination of frictional slip and viscous flow; Fig. 3) such that  
93 differential stress in the upper crust is relaxed to re-establish the “at yield” condition (Fig.

94 3c). As both frictional and viscous components of the fault system undergo the same overall  
95 strain, they operate in parallel (A, B in Fig. 3b). As long as surface uplift since extension  
96 began is proportional to elevation,  $h$ , which as explained in the Methods is a reasonable  
97 assumption<sup>10,12</sup>, the increase in differential stress is independent of depth and simply  
98 proportional to  $\rho gh$  ( $\rho$  is crustal density;  $g$  is acceleration due to gravity). This reasoning,  
99 which requires that buoyancy forces rather than plate boundary forces are the dominant  
100 control on upper crustal deformation, explains the spatial variation in regional strain rates,  
101 provides the link between the relationship shown in Fig. 1(d) and Equation 1, and thereby  
102 allows us to constrain the exponent  $n \approx 3$ . Other studies that compare topography with strain  
103 rates derived from fault slip and geodetic data<sup>16</sup> assume  $n \approx 3$  to explain their data but here,  
104 for the first time, we use such data to constrain its value.

105         Our surface strain rate measurements are derived from slip along faults so they do not  
106 represent deformation of a continuum. For example, at the scale of individual fault blocks  
107 (20km x 20km; Fig. 2a) the spatial gradients in strain rate and mean elevation (Fig. 2b) co-  
108 vary, consistent with the regional relationship (Fig. 1), but the correlation between  $\dot{\epsilon}$  and  $h$  is  
109 poor ( $R^2 < 0.5$ ) because of the heterogeneous pattern of brittle faulting. However, is viscous  
110 deformation at depth also likely to be heterogeneous, as proposed in Fig. 3(a)? Deforming  
111 non-linear viscous materials (i.e.  $n > 1$ ), in general, show a tendency to localise strain and the  
112 development of a brittle fault up-dip provides a geometrical discontinuity that influences  
113 where in the viscous regime localisation preferentially develops<sup>22</sup>. Brittle-frictional faults  
114 extending down to depths of at least 10km in this area are revealed by earthquake  
115 aftershocks<sup>21</sup>. During major earthquakes, cataclasis, hydrous alteration and shear heating  
116 together contribute to grain size reduction and material weakening<sup>8</sup>, processes associated with  
117 localisation at the frictional-viscous transition<sup>23</sup> (Fig. 3) and enhanced shear zone

118 development within the viscous regime down-dip of seismogenic faults<sup>24</sup>. We also know that  
119 fine grained, poly-mineralic, mylonitic shear zones remain weaker<sup>23</sup> and deform at higher  
120 strain rates than surrounding coarser grained less deformed rock (red line, Fig. 3a) and  
121 contribute to lowering the effective viscosity (Fig. 1d)<sup>25</sup>.

122 In the mid- to lower crust quartzo-feldspathic mylonites form a fabric of mineral  
123 segregated layers parallel to shear so that their strength is controlled by the weakest phase:  
124 quartz. Using a flow law for wet quartz calibrated for mylonitic rocks<sup>26</sup> to fit measured strain  
125 rates across brittle fault zones (~5 km wide)<sup>9</sup>, we estimate a lower bound on the temperature,  
126  $T$ , of the viscously deforming material to be  $710 \pm 120\text{K}$  ( $\sim 440 \pm 120^\circ\text{C}$ ). These temperatures  
127 are reached just below the base of the seismogenic zone ( $25 \pm 7.5$  km), as constrained by  
128 surface heat flow data<sup>15</sup> and upper crustal seismicity<sup>19,21</sup> (see Methods). At the 99%  
129 confidence level the exponent we derive is consistent with this flow law (Fig. 1d) as well as  
130 with recent theoretical predictions of shear zone rheology<sup>27</sup> and textural evidence<sup>8,23,25,26,27</sup>  
131 from poly-mineralic mylonitic rocks. We suggest therefore that the rate of viscous flow in  
132 shear zones dominates over distributed flow within the lower crust and/or upper mantle and  
133 regulates the slip rate we measure over long timescales on the up-dip seismogenic part of the  
134 fault even if on shorter time scales rupture depends on elastic loading and mechanical  
135 instabilities<sup>3,4</sup>.

136 The relationship between  $\dot{\epsilon}$  and  $h$  (Fig. 1d) also permits the controls on regional  
137 seismic hazard to be re-evaluated. Uplift of the Italian Peninsula has been on-going since at  
138 least the Quaternary, fast enough in places to raise Plio-Pleistocene marine sediments by over  
139 400 m since the Early Pleistocene<sup>10,28,29</sup>. Contemporary surface uplift, documented by  
140 geodetic levelling lines across both the footwalls and hanging-walls of active faults, indicates  
141 regional uplift of 0–0.5 mm/yr close to the coasts, increasing to 1.0–1.5 mm/yr inland<sup>13</sup>.

142 Furthermore, slip rates along the largest normal faults in the highest elevation areas of central  
143 Italy (Fig. 2a) increased significantly  $\sim 0.8\text{-}1\text{Ma}^{30}$ . Some hanging-wall basins became  
144 internally drained<sup>12</sup> in part because of high rates on basin-bounding faults, consistent with  
145 progressive strain localisation<sup>14,30</sup>. Although recent analysis of geodetic data and instrumental  
146 seismicity suggests that active deformation may be localised in a zone only  $\sim 50\text{km}$  wide<sup>14</sup>  
147 (Fig. 4), historical earthquake shaking records (since 1349 A.D.) and the distribution of  
148 Holocene scarps imply a broader active zone  $80\text{-}90\text{km}$  wide (Fig. 4). These apparently  
149 contradictory observations become consistent when viewed in the light of the derived  
150 relationship (Fig. 1d) as it predicts that strain rate decreases rapidly across strike from the  
151 highest elevation areas towards the coast (Fig. 4) and smaller strains are more readily  
152 resolved when observed over a longer period of observation ( $10^2\text{-}10^4$  yr versus  $< 10^1$  yr in  
153 this case).

154 In summary, rates of seismicity on frictional faults in this example are regulated by  
155 rates of localised viscous flow at depth constrained for the first time by observations averaged  
156 over the timescale of multiple earthquake cycles and likely representing the *in situ* and long-  
157 term ( $10^4$  years) mechanical properties of deforming mylonitic shear zones.

## 158 **Methods:**

159 **Strain rate calculation:** Reference 9 presents the calculations used to convert field  
160 measurements of the direction and amount of Holocene fault slip (since  $15\pm 3$  ka) into strain-  
161 rates within grid cells, the dimensions of which can be specified and thus varied. Fig. 2(a)  
162 shows principal extensional strain rates (blue bars) calculated using this approach for  $20\text{ km} \times$   
163  $20\text{ km}$  grid cells for the central Apennines. The strain rate calculations follow established  
164 methods. For details see Supplementary material. To obtain the strain rate data shown in Fig.  
165 1 the principal extensional strain rate is first calculated using a  $5\text{ km} \times 5\text{ km}$  grid oriented



166 NE-SW, approximately parallel to the principal strain orientation (043°-223°), extending a  
167 distance 90 km across strike. From these data we calculate the strain rate in adjacent  
168 rectangular regions 5km x 90km (see Fig. S1 in Supplementary material). We combine  
169 together adjacent 5km x 90km regions to obtain independent estimates of the principal strain  
170 rate in transects of a given width (10km, 20km, 30km etc.; Fig. S2) over the whole study  
171 area. Transects 30km wide suppress short length scale variations due to fault displacement  
172 gradients and constrain well the regional variations in strain rate along strike along the Italian  
173 Apennines from NW to SE (see Fig. S2). To characterise shorter wavelength spatial  
174 variations in strain rate and elevation across strike across the central Apennines we calculate  
175  $\Delta\dot{\epsilon} / \Delta x$  and  $\Delta h / \Delta x$  (Fig. 2b), by taking the difference in strain-rate ( $\Delta\dot{\epsilon}$ ) and mean elevation  
176 ( $\Delta h$ ) between adjacent 20 km x 20 km cells (Fig. 2a) along the extension direction (043°-  
177 223°), from NE to SW, and dividing by  $\Delta x = 20$  km.

178

179 **Topographic data and stress:** To calculate elevation (Fig. 1) topographic profiles located  
180 along the centre of 5 km x 90 km regions (see strain rate calculation) were constructed from  
181 SRTM 90 m DEM data using GeoMapApp. Each of the topographic data profiles are  
182 orientated NE–SW and are separated along-strike by 5 km intervals. Spot heights along the  
183 topographic profiles are sampled approximately every 850 m. The 5 km width transects were  
184 combined to calculate the mean elevation within wider transects (10km, 20km, 30km etc.) to  
185 derive regional elevation variations along strike. The 95% confidence intervals of the mean  
186 elevation are calculated using the assumption of a normal distribution in the topographic spot  
187 heights<sup>10</sup>. Remnants of a flat palaeolandscape, formed close to sea-level during the Pliocene  
188 and now identified at high elevations, plus preservation of uplifted marine deposits and  
189 terraces indicate that the present day topography has mainly formed since extension began<sup>10</sup>.  
190 Subsequent erosion/deposition is minimal and many of the high elevation hanging-wall

191 basins remain unincised<sup>12</sup>. See Supplementary material for more details. Stress (MPa) and  
192 effective viscosity ( $\eta = \sigma/2\dot{\epsilon}$ ) (top axis in Fig. 1d) are derived using  $\sigma = \rho gh$  where  $\rho = 2800$   
193  $\text{kgm}^{-3}$  and  $h$  = elevation in meters.

194

195 **Correlation between strain rate and elevation:** Grey lines in Fig. 1d are best fit regressions  
196 through data obtained by sampling mean elevation,  $h$ , and strain rate,  $\dot{\epsilon}$ , in 30 km wide  
197 transects (90km across strike). Data from two transect positions (offset by 15 km) are  
198 presented to demonstrate there is no selection bias. Regressions lines (Fig. 1d) are given by:  $\dot{\epsilon}$   
199  $= 10^{-17.8} h^{3.2}$  with  $R^2 = 0.8$  ( $1\sigma$ ) and  $\dot{\epsilon} = 10^{-17.9} h^{3.3}$  with  $R^2 = 0.9$  ( $1\sigma$ ). The estimate of the  
200 power law exponent depends on transect width; 30 km wide transects best constrain its value  
201 (see Fig. S2). The six different transect positions at this scale yield a value of the exponent in  
202 the range 3.0 to 3.3 and a pre-factor of  $10^{-17.6+0.3-0.9}$ . We use  $\dot{\epsilon} = 10^{-17.6} h^{3.2}$  in Figure 4 to  
203 predict the variation in strain rate from topography.

204 **Temperature-depth calculation:** We use values for  $Q$ ,  $\log A$ ,  $R$  and  $n$  (Eqn. 1) from a flow  
205 law for wet quartz<sup>26</sup> and solve for the temperature  $T$  that predicts strain rates of similar  
206 magnitude to those measured across 5 km wide fault zones<sup>9</sup>.  $Q = 135 \pm 15$  kJ/mol,  $\log A = -$   
207  $11.2 \pm 0.6$  MPa<sup>-n</sup>/s,  $R = 8.314472$  m<sup>2</sup> kg s<sup>-2</sup> K<sup>-1</sup> mol<sup>-1</sup>,  $n = 4$ . We obtain  $T = 710 \pm 120$  K, i.e.,  
208  $\sim 440 \pm 120^\circ\text{C}$ . Average surface heat flow of  $50$  mWm<sup>-2</sup> in this area<sup>15</sup> is used to derive  
209 temperature versus depth through the upper crust assuming a surface temperature of  $10^\circ\text{C}$ ,  
210 crustal heat production =  $1 \times 10^{-6}$  Wm<sup>-3</sup> and thermal conductivity =  $2.5$  J s<sup>-1</sup> m<sup>-1</sup> K<sup>-1</sup>.  
211 Following the standard approach, crustal heat production decreases exponentially with depth  
212 (characteristic depth = 10 km). The inferred depth range of viscous flow implied by the  
213 temperature range is  $25 \pm 7.5$  km, i.e., below the depth extent of upper crustal seismicity (14-

214 17 km<sup>19,21</sup>). As mantle lithosphere is thinned in this region, extrapolating this temperature  
215 depth profile may underestimate lower crust/upper mantle temperatures.

216

## 217 **References**

- 218 1. Thatcher, W. Nonlinear strain build up and the earthquake cycle on the San Andreas  
219 Fault, *J. Geophys. Res.*, **88**, 5893–5902 (1983).
- 220 2. Bürgmann, R. & Dresen, G. Rheology of the lower crust and upper mantle: Evidence  
221 from rock mechanics, geodesy and field observations. *Ann. Rev. Earth Planet. Sci.*, **36**,  
222 531–567 (2008).
- 223 3. Kenner, S. J. & Simons, M. Temporal clustering of major earthquakes along individual  
224 faults due to post-seismic reloading, *Geophys. J. Int.*, **160**, 179-194 (2005).
- 225 4. Freed, A. M. Earthquake triggering by static, dynamic and postseismic stress transfer,  
226 *Ann. Rev. Earth Planet Sci.* **33**, 335-367 (2005).
- 227 5. Carter, N. L. & Tsenn, M. C. Flow properties of continental lithosphere. *Tectonophysics*,  
228 **136**, 27–63 (1987).
- 229 6. Newman R. & White N. The dynamics of extensional sedimentary basins: constraints  
230 from subsidence inversion, *Philos. Trans. R. Soc. Lond.* **357**, 805– 830, (1999).
- 231 7. Freed, A. M. & Bürgmann, R. Evidence of power law flow in the Mojave Desert mantle.  
232 *Nature*, **430**, 548–551 (2004).
- 233 8. Handy, M. R., Hirth, G. & Bürgmann, R. Continental fault structure and rheology from  
234 the frictional viscous transition downward. In: *Tectonic Faults: Agents of Change on a*  
235 *Dynamic Earth*. (Edited by: Handy, M. R., Hirth, G. and Hovius, N.). MIT Press  
236 Cambridge Massachusetts, London, UK, pp. 139–181 (2007).

- 237 9. Faure Walker, J.P., Roberts, G.P., Sammonds, P.R., & Cowie, P. A. Comparison of  
238 earthquake strains over  $10^2$  to  $10^4$  year timescales: Insights into variability in the seismic  
239 cycle in central Apennines, Italy., *J. Geophys. Res.*, **115**, B10418, (2010).
- 240 10. Faure Walker, J. P., Roberts, G. P., Cowie, P. A., Papanikolaou, I., Michetti, A. M.,  
241 Sammonds, P., Wilkinson, M., McCaffrey, K.J. & R.J. Phillips, Relationship between  
242 topography and strain rate in the actively extending Italian Apennines. *Earth Planet. Sci.*  
243 *Lett.*, **325/326**, 76–84, (2012).
- 244 11. Roberts, G. P. & Michetti, A. M. Spatial and temporal variations in growth rates along  
245 active normal fault systems: an example from The Lazio–Abruzzo Apennines, central  
246 Italy. *J. Struct. Geol.*, **26**, 339–376 (2004).
- 247 12. D'Agostino, N., Jackson, J., Dramis, F., Funiciello, R. Interactions between mantle  
248 upwelling, drainage evolution and active normal faulting: an example from the central  
249 Apennines (Italy). *Geophys. J. Int.* **147**, 475–497 (2001).
- 250 13. D'Anastasio, E., De Martini, P.M., Selvaggi, G., Pantosti, D., Marchioni, A. & Maseroli,  
251 R. Short-term vertical velocity field in the Apennines (Italy) revealed by geodetic  
252 levelling data. *Tectonophysics*, **418**, 219–234 (2006).
- 253 14. D'Agostino, N., Mantenuto, S., D'Anastasio, E., Giuliani, R., Mattone, M., Calcaterra,  
254 M., Gambino, P., and Bonci, L. Evidence for localized active extension in the central  
255 Apennines (Italy) from global positioning system observations. *Geology*, **39**, 291–294,  
256 (2011).
- 257 15. Della Vedova, B., Bellani, S., Pellis G. & Squarci, P. Deep temperatures and surface heat  
258 flow distribution, in *Anatomy of an Orogen: The Apennines and adjacent Mediterranean*  
259 *Basins* (eds. G. B. Vai & I. P. Martini). Kluwer Academic Publishers. pp. 65-76 (2001).
- 260 16. England, P. & Molnar, P. Late Quaternary to decadal velocity fields in Asia. *J. Geophys.*  
261 *Res.*, **110**, B12401 (2005).

- 262 17. Flesch, L. & Bendick, R. The relationship between surface kinematics and deformation of  
263 the whole lithosphere. *Geology*, 40, 711-714 (2012).
- 264 18. Naliboff, J. B., Lithgow-Bertolloni, C., Ruff, L. J. & de Koker, N. The effects of  
265 lithospheric thickness and density structure on Earth's stress field. *Geophys. J. Int.*, **188**,  
266 1–17 (2008).
- 267 19. Boncio, P., Tinari, D. P., Lavecchia, G., Visini, F. & Milana, G. The instrumental  
268 seismicity of the Abruzzo Region in Central Italy (1981-2003): seismotectonic  
269 implications, *Ital.J.Geosci.* (Boll.Soc.Geol.It.), **128**, 367-380, (2009).
- 270 20. Jaeger, J. C. & Cook, N.G. Fundamentals of rock mechanics, 2<sup>nd</sup> Edition, Chapman &  
271 Hall, London, 593 pp. (1979).
- 272 21. Chiarabba, C. and 28 co-authors. The 2009 L'Aquila (central Italy)  $M_w$ 6.3 earthquake:  
273 Main shock and aftershocks. *Geophys. Res. Let.*, **36**, L18308 (2009).
- 274 22. Huismans, R.S. & Beaumont, C. Roles of lithospheric strain softening and heterogeneity in  
275 determining the geometry of rifts and continental margins, *In* Karner, G.D., Manatschal, G., &  
276 Pinheiro, L.M. (eds) Imaging, Mapping and Modelling Continental Lithosphere Extension and  
277 Breakup, pp. 107-134. *Geol. Soc. Lond. Spec. Pub.*, **282**, (2007).
- 278 23. Fusseis, F., Handy, M. R. & Schrank. Networking of shear zones at the brittle-to-viscous  
279 transition (Cap de Creus, NE Spain), *J. Struct. Geol.*, **28**, 1228-1243 (2006).
- 280 24. Ellis, S. & Stöckhert, B. Imposed strain localization in the lower crust on seismic  
281 timescales, *Earth Planets Space*, **56**, 1103-1109, (2004).
- 282 25. Mehl, L. & Hirth, G. Plagioclase recrystallization and preferred orientation in layered  
283 mylonites: Evaluation of flow laws for the lower crust, *J. Geophys. Res.*, **113**, B05202,  
284 (2008).

- 285 26. Hirth, G., Teyssier, C. & Dunlap, W.J. An evaluation of quartzite flow laws based on  
286 comparisons between experimentally and naturally deformed rocks, *Int. J. Earth Sci.*,  
287 (Geologische Rundschau), **90**, 77-87 (2001).
- 288 27. Platt, J. P. & Behr, W. M. Grainsize evolution in ductile shear zones: Implications for  
289 strain localisation and the strength of the lithosphere. *J. Struct. Geol.*, **33**, 537-550 (2011).
- 290 28. Gliozzi, E. & Mazzini, I. Paleoenvironmental analysis of Early Pleistocene brackish  
291 marshes in the Rieti and Tiberino intraappenninic basins (Latium and Umbria, Italy)  
292 using ostracods (Crustacea). *Palaeogeogr. Palaeoclimatol. Palaeoecol.* 140, 325–333  
293 (1998).
- 294 29. Mancini, M. D'Anastasio, E., Barbieri, M. & De Martini, P-M. Geomorphological,  
295 paleontological and  $^{87}\text{Sr}/^{86}\text{Sr}$  isotope analyses of early Pleistocene paleoshorelines to  
296 define the uplift of Central Apennines (Italy). *Quaternary Research*, **67**, 487–501 (2007).
- 297 30. Roberts, G. P., Michetti, A., Cowie, P. A., Morewood, N. C. & Papanikolaou, I. Fault  
298 Slip-Rate Variations During Crustal-Scale Strain Localisation, Central Italy. *Geophys.*  
299 *Res. Lett.*, **29**, 1168, (2002).

300

301 **Supplementary Information:**

302 Section 1: Summary of main calculation steps used in strain rate calculations plus evaluation  
303 of sources and magnitudes of uncertainties.

304 Section 2: Estimate of power law exponent relating strain rate to elevation using different  
305 transect widths and positions including an analysis of confidence intervals on these estimates.

306 Section 3: Comparing depth extent of active seismicity to inferred depth of viscous flow for  
307 different values of surface heat flow measured in the Italian Apennines.

308

309 Correspondence and requests for materials should be addressed to P.A. Cowie

310 ([patience.cowie@geo.uib.no](mailto:patience.cowie@geo.uib.no))

311

312 **Acknowledgements.** N. D'Agostino supplied the long wavelength topography data used in

313 Figs. 2 and 4. This work was supported by NERC grants: NER/S/A/2006/14042,

314 NE/E01545X/1 and NE/I024127/1. Financial support was also provided by the Statoil Earth

315 System Modelling project (P.S.) and the Statoil-University of Bergen Akademia agreement

316 (P.C.). We thank R. Huisman for useful discussions and P. Molnar, M. Handy and an

317 anonymous reviewer for their comments.

318

319

320

321

322

323

324

325

326 **Author contribution statement:**

327 **PAC** led the interpretation of the scaling exponent in terms of mid-crustal shear zones.

328 **CHS** contributed to understanding the behaviour of coupled frictional-viscous fault systems.

329 **GPR** provided the structural data and analysed the strain rate vs elevation relation.

330 **JFW** performed the strain rate calculations and quantified data uncertainties.

331 **PS** contributed to understanding stress and strain rate variations in a layered lithosphere.

332

333 **Figure 1. Correlation between Holocene-averaged regional extensional strain rates and**  
334 **mean elevation along the Italian Apennines.** (a) Location map, (b) fault pattern overlying  
335 SRTM DEM, (c) strain rate (red) and elevation (black) versus distance measured every 10 km  
336 in 90 km transects across strike. Shading indicates  $1\sigma$  error. (d) Log-log plot of  $h$ , stress  
337 (MPa), effective viscosity ( $\eta = \sigma/2\dot{\epsilon}$ ), versus  $\dot{\epsilon}$  for two independent data sets (triangles,  
338 diamonds), offset by 15km along strike, using 30km wide transects. Grey lines: best fit power  
339 laws ( $1\sigma$  error). Grey dashed lines: 99% CI for all transect widths and positions (see  
340 Supplementary material).

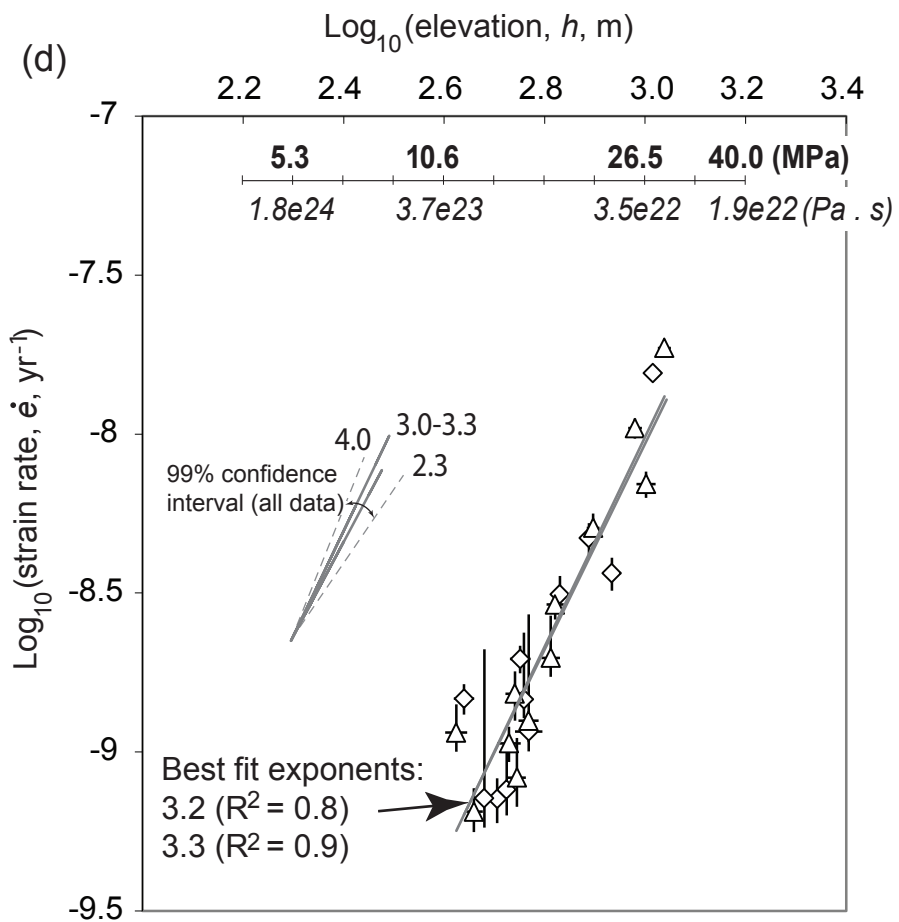
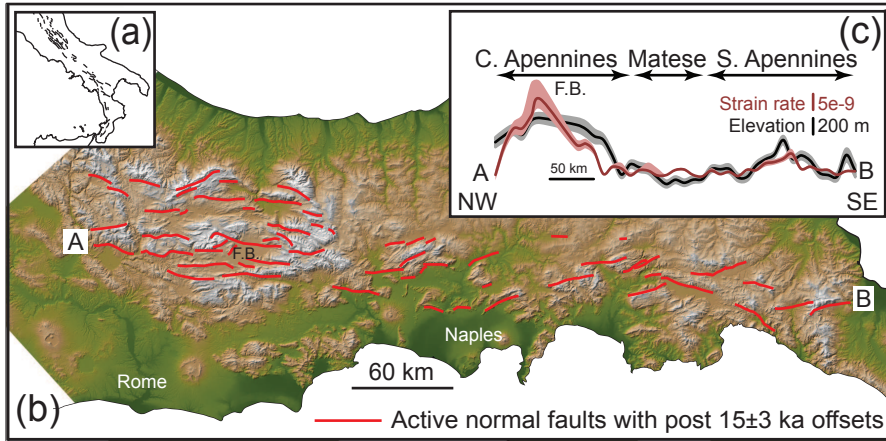
341 **Figure 2. Spatial variation in strain rate with elevation across the central Apennines**  
342 **(Abruzzo).** (a) Pattern of normal faults (red lines) superimposed on long wavelength  
343 topography (m) (black contours). Grey shading  $>800$  m. Thick red lines: faults where  
344 Holocene slip rate exceeds long term rate<sup>30</sup>. Holocene extensional strain rates (blue bars) in  
345 grid cells  $20\text{ km} \times 20\text{ km}$ <sup>9</sup>. Grid orientated parallel to principal strain axes. (b) Topographic  
346 slope vs. change in strain rate (black dots) between adjacent 20 km grid cells along the  
347 maximum extension orientation from NE to SW; open circles indicate where a cell contains  
348 no faults.

349 **Figure 3. Rheology and loading of a coupled frictional-viscous fault system.** (a)  
350 Schematic fault geometry and rheological structure. FVT = Frictional-Viscous Transition.  
351 Strain rate enhancement (red line) depends on shear zone width (5 km assumed here). (b)  
352 Brittle-frictional-viscous components loaded in parallel by a driving stress that depends on  
353 elevation,  $h$ . Both components may deform elastically on short time scales. Frictional element  
354 A represents (collectively) the seismogenic faults, viscous element B the corresponding  
355 viscous (mylonitic) shear zones. (c) Distribution of crustal stress (and strength) at yield and  
356 the increase in differential stress, due to regional uplift, which leads to deformation.



357 **Figure 4. Contemporary strain accumulation across Abruzzo.** Width of high strain rate  
358 zone (along line shown in Fig. 2a) implied by geodesy<sup>14</sup> (red arrow) (current resolution:  $\dot{\epsilon} \geq 2$   
359  $\times 10^{-8}$ ) versus fault scarp mapping (blue arrow) (estimated resolution:  $\dot{\epsilon} \geq 5 \times 10^{-9}$ ). Strain rate  
360 variation (grey line) predicted from long wavelength topography<sup>14</sup> (thick black line) using  $\dot{\epsilon} =$   
361  $10^{-17.6} h^{3.2}$  (see Methods). Thin black line: SRTM topography. Stars indicate locations of  
362 large historical earthquakes (1915 Fucino  $M_s = 7.0$  and 2009 L'Aquila  $M_w = 6.3$ ). Dashed  
363 line: width of active zone inferred from earthquake shaking records since 1349.

364



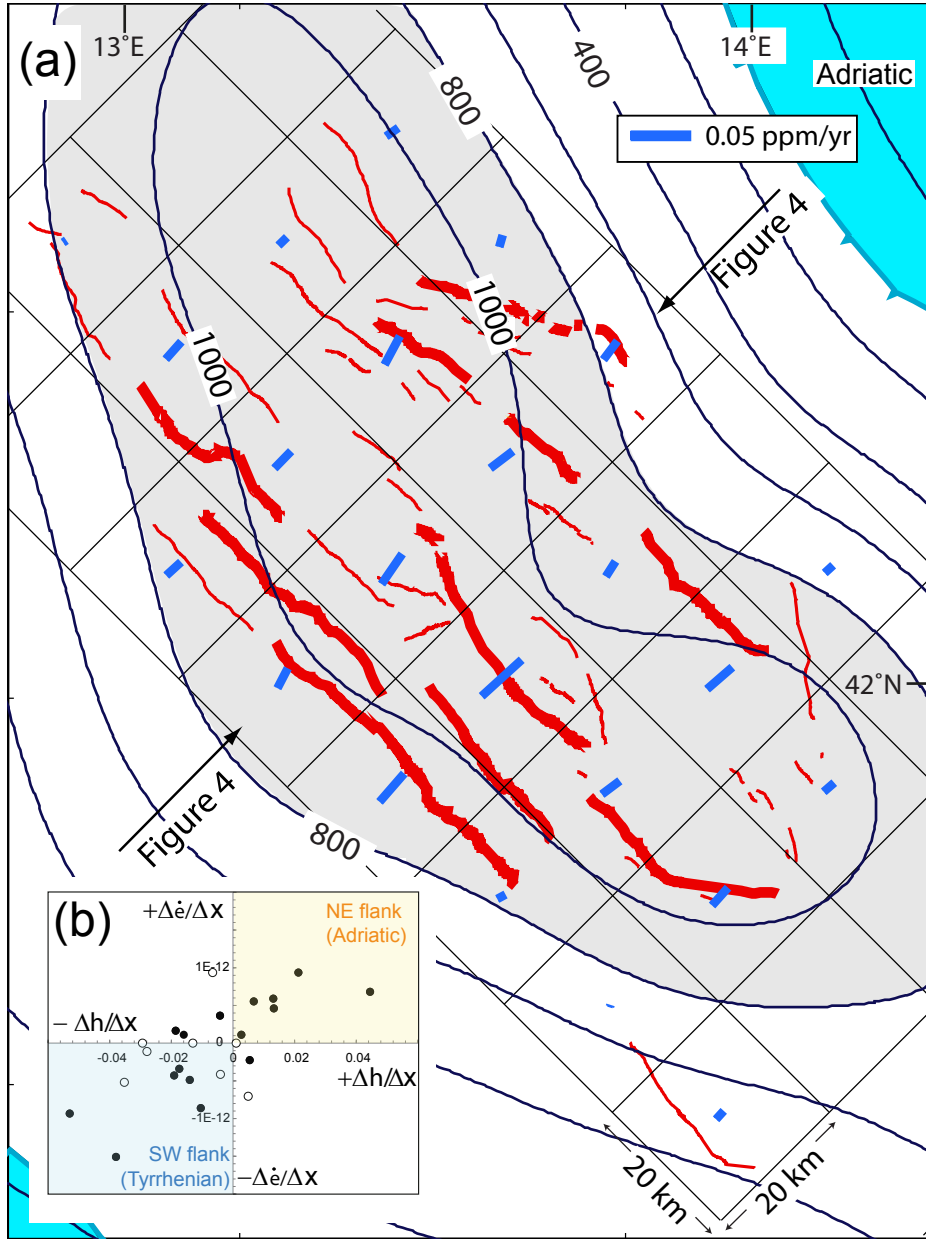


Figure 2

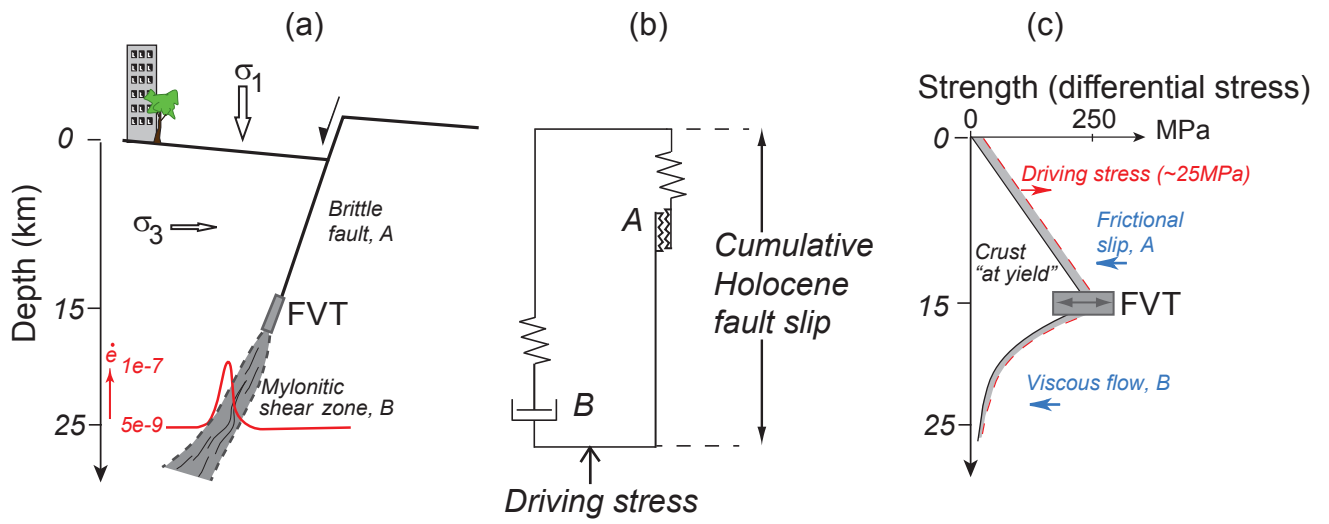


Figure 3

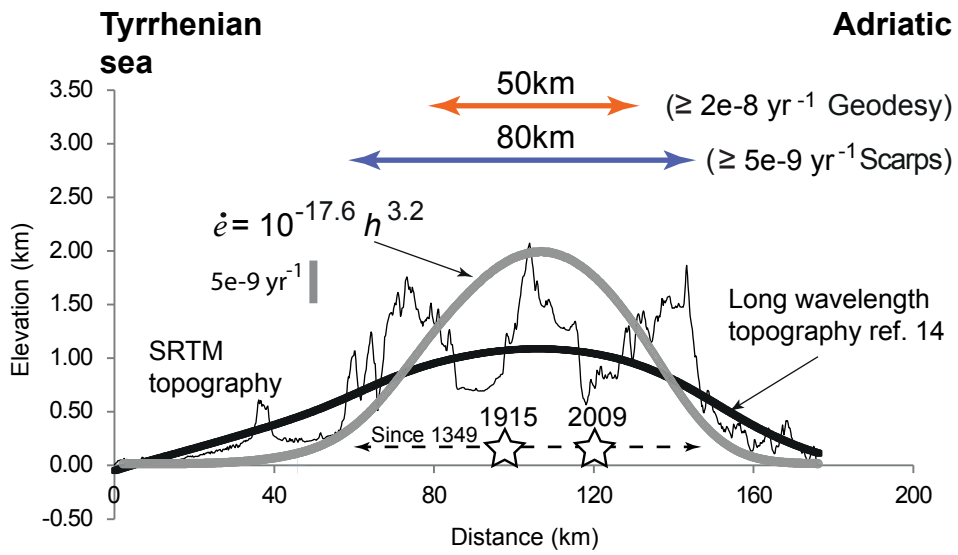


Figure 4